NeuroImage: Clinical 37 (2023) 103327

Contents lists available at ScienceDirect

NeuroImage: Clinical

journal homepage: www.elsevier.com/locate/ynicl

Hippocampal subfield viscoelasticity in amnestic mild cognitive impairment evaluated with MR elastography

Peyton L. Delgorio [a], Lucy V. Hiscox [a], Grace McIlvain [a], Mary K. Kramer [a], Alexa M. Diano [a], Kyra E. Twohy [b], Alexis A. Merritt [a], Matthew D.J. McGarry [c], Hillary Schwarb [d], Ana M. Daugherty [e], James M. Ellison [f,g], Alyssa M. Lanzi [g], Matthew L. Cohen [g], Christopher R. Martens [h], Curtis L. Johnson [a,b,*]

[a] Department of Biomedical Engineering, University of Delaware, Newark, DE, United States
[b] Department of Mechanical Engineering, University of Delaware, Newark, DE, United States
[c] Thayer School of Engineering, Dartmouth College, Hanover, NH, United States
[d] Beckman Institute for Advanced Science and Technology, University of Illinois at Urbana-Champaign, Urbana, IL, United States
[e] Department of Psychology and Institute of Gerontology, Wayne State University, Detroit, MI, United States
[f] Swank Memory Care and Geriatric Consultation, ChristianaCare, Wilmington, DE, United States
[g] Department of Communication Sciences and Disorders, University of Delaware, Newark, DE, United States
[h] Department of Kinesiology and Applied Physiology, University of Delaware, Newark, DE, United States

ARTICLE INFO

Keywords:
Brain
Hippocampus
Mild Cognitive Impairment
Neurodegeneration
Mechanical Properties
Stiffness

ABSTRACT

Hippocampal subfields (HCsf) are brain regions important for memory function that are vulnerable to decline with amnestic mild cognitive impairment (aMCI), which is often a preclinical stage of Alzheimer's disease. Studies in aMCI patients often assess HCsf tissue integrity using measures of volume, which has little specificity to microstructure and pathology. We use magnetic resonance elastography (MRE) to examine the viscoelastic mechanical properties of HCsf tissue, which is related to structural integrity, and sensitively detect differences in older adults with aMCI compared to an age-matched control group. Group comparisons revealed HCsf viscoelasticity is differentially affected in aMCI, with CA1-CA2 and DG-CA3 exhibiting lower stiffness and CA1-CA2 exhibiting higher damping ratio, both indicating poorer tissue integrity in aMCI. Including HCsf stiffness in a logistic regression improves classification of aMCI beyond measures of volume alone. Additionally, lower DG-CA3 stiffness predicted aMCI status regardless of DG-CA3 volume. These findings showcase the benefit of using MRE in detecting subtle pathological tissue changes in individuals with aMCI via the HCsf particularly affected in the disease.

1. Introduction

Alzheimer's disease (AD) is a debilitating neuropathological condition characterized clinically by memory impairment and decline of additional cognitive functions. AD results in widespread neurodegeneration that is associated with progressive accumulation of amyloid plaques and tau protein misfolding and the buildup of neurofibrillary tangles (Petersen, 2004; Petersen et al., 1999). Amnestic mild cognitive impairment (aMCI) is often an early manifestation of AD where clinical cognitive impairment is detectable and AD pathology is present, but prior to the significant neurodegeneration and functional decline marking later AD (Albert et al., 2011; Gauthier et al., 2006). The hippocampus (HC) has an important functional role in memory formation and retrieval (Du et al., 2006; Pennanen et al., 2004; Petersen et al., 2000) and is a site that preferentially harbors AD pathology and is structurally affected during the early symptomatic stages of the disease (Gauthier et al., 2006; Mueller and Weiner, 2009). However, the HC is a heterogeneous structure that is not affected uniformly across AD progression (de Flores et al., 2015), and thus studying the whole HC may be less sensitive in differentiating structural differences between aMCI and healthy controls. Therefore, to sensitively capture the differential effects of each AD stage on the HC microstructure, it is important to understand how the subregions of the HC are specifically affected to improve our ability to diagnose AD and track disease progression.

* Corresponding author at: Department of Biomedical Engineering, University of Delaware, 540 S College Ave, Newark, DE 19713, United States.
E-mail address: clj@udel.edu (C.L. Johnson).

https://doi.org/10.1016/j.nicl.2023.103327
Received 8 August 2022; Received in revised form 6 January 2023; Accepted 16 January 2023
Available online 18 January 2023

The HC is a non-uniform structure comprising subfields with cytoarchitecturally unique regions that differ in the vasculature and electrophysiological properties (Duvernoy, 2005; Lavenex and Lavenex, 2013). The HC subfields (HCsf) include the dentate gyrus (DG), cornu ammonis 1–3 (CA1-3), and the subiculum (SUB), as well as an interface connecting the HC to the neocortex known as the entorhinal cortex (ERC) (Duvernoy, 2005). Prior volumetric studies, focusing on both aMCI and AD, revealed differential volume loss in the HCsf, suggesting specific subfields may also be affected before other HC subregions in the diseases (Du et al., 2001; Mueller et al., 2010). Specifically, CA1-CA2 volumetry has previously shown vulnerability to aMCI, vascular pathology, and AD-related genetic variations, with studies suggesting it may be a more accurate diagnostic measure of structural atrophy compared to the whole HC (de Flores et al., 2015; Kerchner et al., 2014; Mueller and Weiner, 2009; Wisse et al., 2014). Additionally, biological hallmarks, such as amyloid-beta deposition, are associated with tissue atrophy and structural degeneration in aMCI and AD progression (Breijyeh and Karaman, 2020; Gauthier et al., 2006). In the HCsf, amyloid pathology and distribution appear to affect the CA1 region before the other regions (Braak and Braak, 1991), while a decrease in neuronal firings to the DG from the ERC is associated with more dense amyloid distribution (Reilly et al., 2003). Imaging techniques sensitive to HCsf tissue microstructure and pathology can improve detection of aMCI and potentially the progression to AD.

Magnetic resonance elastography (MRE) is a sensitive, noninvasive neuroimaging technique that can quantify brain tissue viscoelasticity. Viscoelastic properties reflect brain tissue microstructural integrity, representing the organization and distribution of neuronal, axonal, and glial cells and extracellular matrix in the brain (Freimann et al., 2013; Klein et al., 2014; Riek et al., 2012; Schregel et al., 2012). Aging and neurodegeneration have been shown to lead to loss of tissue structural integrity, as reflected by a decline in brain viscoelastic properties (Hiscox et al., 2018, 2020a). Previous MRE studies have also revealed that AD is associated with greater softening of brain tissue, particularly in regions known to be affected by AD pathology (Gerischer et al., 2018; Hiscox et al., 2020a; Murphy et al., 2011, 2016). Currently, only one MRE study has investigated the association of MCI with changes in brain tissue viscoelasticity, focusing specifically on stiffness changes in large lobar regions (Murphy et al., 2016). However, as the HC and the HCsf are strongly affected by the Alzheimer's pathology, it is important to examine viscoelastic changes in these regions in aMCI. Our group has previously shown the sensitivity of MRE in detecting structural differences of the HC in aging and neurodegeneration (Delgorio et al., 2021; Hiscox et al., 2018; Johnson et al., 2016b), and have recently developed a high-resolution, MRE protocol to reliably measure the viscoelasticity of individual HCsf (Delgorio et al., 2022, 2021), which can be potentially more sensitive to aMCI by examining the neural substrates first affected by the underlying pathology of aMCI.

In this work, we used a high-resolution MRE protocol to measure viscoelasticity mechanical properties of HCsf tissue in older adults with and without aMCI. Our overarching goal was to test whether viscoelastic property differences exist between healthy older adults and those with aMCI. We also wanted to test whether individual HCsf viscoelastic properties are differentially vulnerable to aMCI, and to determine if the MRE metrics provide additional information about HCsf structural decline in aMCI beyond traditional volumetric measures of atrophy. Based on prior work, we hypothesized participants with aMCI will experience the largest viscoelastic property differences in the CA1-CA2 region, as this region is affected first in the disease (Mueller and Weiner, 2009; Pluta et al., 2012). Overall, this work sought to test whether HCsf MRE measures are valid imaging biomarkers of disease and neurodegeneration.

2. Materials and methods

2.1. Participant recruitment and inclusion criteria

Eighty-three older adults were recruited (age: 60–90 years) to participate in this study, including 20 participants with a diagnosis of aMCI (mean age = 72.7 ± 8.7 years, M/F = 5/15) and 63 cognitively normal (CN) participants (mean age = 69.1 ± 5.4 years, M/F = 19/44). aMCI participants were recruited via flyers, social media advertisements, and direct mailings targeting older adults with self-reported memory complaints. For both groups, potential participants were asked questions to determine if they qualified for the study (e.g., age, general health, ability to undergo MRI testing, etc.). For potential aMCI participants, the *Modified Telephone Interview for Cognitive Status* (TICS-m) was administered over the phone to determine if a participant exhibited a high likelihood of screening positive for aMCI, defined as TICS-m $\leq$ 34 points and $>$ 20 points (maximum score = 51 points) or a low score on the immediate and delayed recall memory sub-tests ($\leq$10) (Cook et al., 2009). Older adults determined to be neurotypical and not likely to have aMCI based on their TICS-m scores and self-reported medical history were eligible to enroll in the study in the CN group. Once potential aMCI participants passed this recruitment stage, they were assessed in person with a neuropsychological test battery comprised of the *Mini-Mental State Exam* (MMSE-2) (Folstein et al., 1983), *Hopkin's Verbal Learning Test-revised* (HVLT-R) (Benedict et al., 1998), and either the *Brief Visuospatial Memory Test* (BVMT) or the *Wechsler Memory Scale (WMS-R) Logical Memory Test*. Individuals were classified as having likely aMCI if they met the following criteria: (A) scored $>$ 21 on the MMSE-2 (Moise et al., 2004; Petersen, 2004), but (B) produced at least one score $<$ -1.5 SD of an age-matched normative sample on either the HVLT-R, BVMT, or WMS-R Logical Memory subtest, and (C) were determined to have a Clinical Dementia Rating (CDR) total score $<$ 1.0 (Morris, 1993) indicating that a reliable informant confirms that the person has some cognitive challenges but not dementia. All screening instruments and the CDR were administered by trained individuals under the supervision of a clinical neuropsychologist on the research team, who also reviewed all cases to confirm aMCI. 182 older adults were considered as likely aMCI based on their phone screen and TICS-m score and invited for in person screening, and subsequently 61 older adults were screened as aMCI. Individuals who were considered likely aMCI based on phone screen, but were not confirmed during in person screening, were not included in this study. Individuals who were confirmed as aMCI during screening may not have enrolled in this study and completed MRI scans for several reasons including contraindications to MRI or lack of interest in the study when enrollment was available. All subjects provided informed, written consent to participate in this study approved by our Institutional Review Board.

2.2. High-Resolution MRE protocol

Each participant underwent an MRI session on a Siemens 3 T Prisma, which included two structural scans: a 0.9 mm^3 T_1-weighted magnetization prepared rapid gradient echo (MPRAGE) and a 0.4x0.4x2.0 mm^3 T_2-weighted turbo spin echo (TSE) scan aligned to the hippocampus; and a high-resolution MRE scan using a 3D multiband, multishot spiral MRE sequence with 1.25 mm isotropic resolution (Johnson et al., 2016a; McIlvain et al., 2022a), which included the following imaging parameters: repetition time/echo time (TR/TE) = 3360/70 ms, 192x192 matrix size, 240 mm × 240 mm field-of-view (FOV), 96 axial slices, with a total scan time of 10 min and 45 s. We used a commercial Resoundant pneumatic actuator (Resoundant, Rochester, MN) to generate shear waves in the brain via vibrations at 50 Hz, with the resulting displacement fields captured by the MRE sequence. A magnetic field inhomogeneity map was separately collected and use to correct distortion during image reconstruction to improve the quality of the displacement information (McIlvain et al., 2022b; Sutton et al., 2003).

HCsf regions were segmented from the TSE scan using Automated Segmentation of Hippocampal Subfields (ASHS) (Yushkevich et al., 2015). The UPenn PMC Atlas was used to provide masks of the individual HCsf regions (CA1, CA2, CA3, DG, SUB, and ERC), which were combined into four regions (DG-CA3, CA1-CA2, SUB, and ERC) to reduce potential MRE property estimation errors in very small regions. Left and right regions were added together to create bilateral, binary segmentation masks and were visually inspected to ensure no overlap was present between the HCsf masks. Additionally, left and right HCsf volumes were obtained and added together to calculate bilateral volume measures for each region. All segmentations were then transformed into MRE space using FMRIB's Linear Image Registration Tool (FLIRT) in FSL and thresholded to create binary masks (Jenkinson et al., 2012; Jenkinson et al., 2002). Segmentations and registrations were manually reviewed at each step for errors.

A nonlinear inversion (NLI) algorithm generated shear stiffness, $\mu = \frac{2|G|^2}{G'+|G|}$, and damping ratio, $\xi = \frac{G''}{2G'}$, property maps, calculated from the complex shear modulus ($G = G' + iG''$) comprising the storage modulus (G') and loss modulus (G'') (McGarry et al., 2012); higher μ and lower ξ indicate better tissue integrity (Hiscox et al., 2021). Additionally, individual HCsf regions were included as spatial priors in the inversion through soft prior regularization (SPR) (McGarry et al., 2013) (Fig. 1). When estimating the HCsf property maps, NLI parameters were optimized to sensitively measure HCsf μ and ξ, using two inversion schemes with the following NLI parameter settings: μ – SPR: $\alpha = 10^{-12}$, spatial filtering (SF) width: 0.9 mm; ξ – SPR: $\alpha = 10^{-12}$, spatial filtering (SF) width: 1.5 mm. See our prior work for complete details of imaging and analysis protocols (Delgorio et al., 2022, 2021). Octahedral shear strain-based signal-to-noise ratio (OSS-SNR) was used to confirm data quality, with all data from all participants over the OSS-SNR threshold of 3.0 considered suitable for NLI (Hannum et al., 2022; McGarry et al., 2011). Population OSS-SNR values in both groups and all HCsf are included in the Supplemental Information (Table S-1).

We also extracted total intracranial volumes (ICV) and whole HC segmentations using FreeSurfer 6.0 (Fischl, 2012) and added left and right segmentations together to create bilateral masks. HC segmentations were transformed into MRE space using FLIRT and thresholded to create binary masks. HC left and right volumes were also obtained from FreeSurfer and added together to generate bilateral HC volumes.

2.3. Statistical analyses

For all models, outliers were detected using a 1.5x interquartile range (IQR) cutoff and were removed accordingly. Additionally, we used the Kolmogorov-Smirnov test to assess data normality for all models (Lilliefors, 1967). To account for subject-specific and group-specific global differences, MRE measures were normalized to global brain μ and ξ, respectively, which has been done in prior MRE work (Murphy et al., 2013). Corrections were performed by adjusting both regional HC and HCsf measures using the analysis of covariance (ANCOVA) approach, which corrects regional measures based on the proportion of the difference between an individual's global brain measure and the average global brain measure for the sample (Eq. (1)) (Jack Jr et al., 1989).

$$RM_{adj} = RM_{raw} - b(GBM_{raw} - \overline{GBM}_{raw}) \quad (1)$$

where RM_{adj} is the covariance-adjusted brain regional measure (HC or HCsf), RM_{raw} is the raw measure for the respective brain region, b is the unstandardized beta weight of the raw brain regional measure regression on raw global brain measure, GBM_{raw} is the global brain raw measure, and $\overline{GBM}_{raw}$ is the sample mean of the raw global brain measures. These adjusted HC and HCsf measures were used for all models. Volume measures were corrected for ICV using the same approach. All statistical analyses were performed using IBM SPSS Statistics version 28.0.0 (IBM Corp., Armonk, N.Y., USA).

2.4. Analysis 1: Differential effects of aMCI on HCsf properties

To establish the value of MRE metrics in detecting property differences between CN and aMCI, we used a one-way ANCOVA model, adjusting for age and sex, to examine HC differences between CN and aMCI participants. Separate μ, ξ, and volume models were run to evaluate group differences between aMCI and CN. To determine the group differences among the HCsf regions, we ran separate general linear

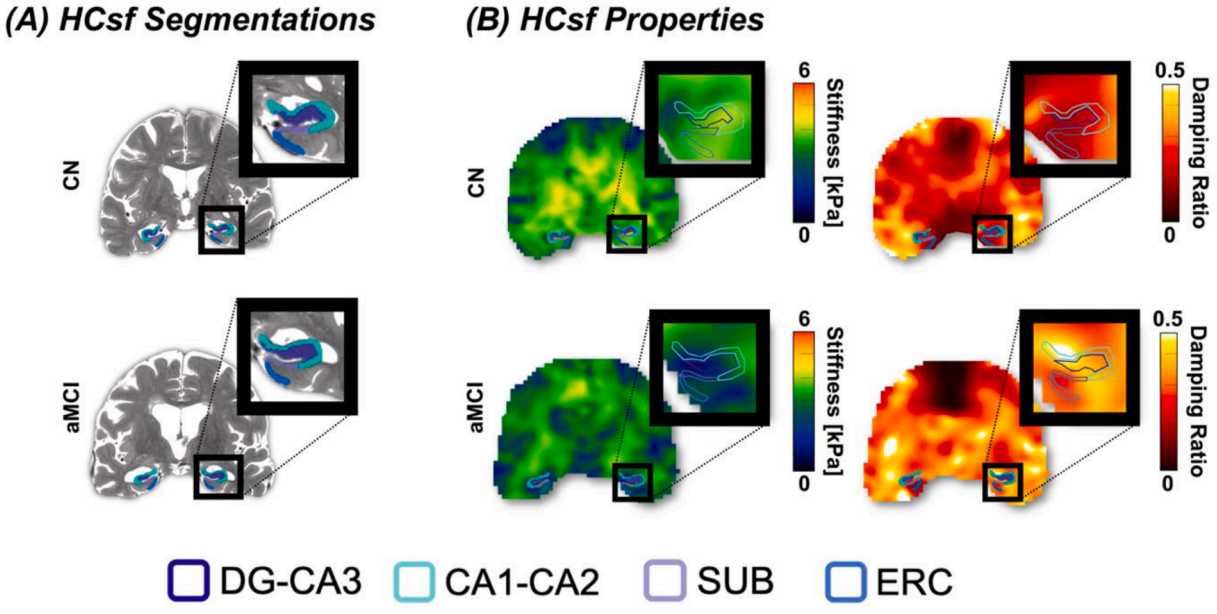

Fig. 1. Overview of the HCsf regions from the MRE Pipeline (Delgorio et al., 2021). (A) Volume Segmentations of the HCsf regions of interest: Dentate Gyrus-Cornu Ammonis 3 (DG-CA3), Cornu Ammonis 1–2 (CA1-CA2), Subiculum (SUB), and Entorhinal Cortex (ERC) using Automated Segmentation of Hippocampal Subfields (ASHS). (B) Generating the shear stiffness and damping ratio property maps. Examples for both MRE metrics are shown for a CN participant (77 y, female) and an aMCI participant (74 y, female).

mixed models (LMM) models, adjusting for age and sex, for HCsf μ, ξ, and volume. These models were used as they allowed us to assess group differences on all HCsf regions in one model. All models used an unstructured residual covariance matrix, which was chosen based on the simultaneous minimization of the Akaike and Bayesian information criteria. We included group, age, and sex as between-subject effects and HCsf region as a 4-level within subject factor. We primarily focused on the group × HCsf interaction, as it tested the hypothesis of specific differential effects of aMCI on the properties of the HCsf regions. *Post-hoc* tests with Bonferroni correction were also performed for each model to determine individual HCsf group differences. Statistical significance was determined at $\alpha = 0.05$.

2.5. Analysis 2: Contributions of HCsf MRE measures in classifying aMCI

We performed stepwise logistic regression analyses, adjusting for age and sex, to determine if HCsf MRE metrics improved classifier performance beyond HCsf volumes in differentiation of aMCI from CN participants. Models were run only for the significant HCsf MRE regions from Analysis 1 – i.e., CA1-CA2 μ, DG-CA3 μ, and CA1-CA2 ξ – where we tested if the addition of the MRE measure improved classifier performance in the model beyond volume of the same corresponding region. Additionally, receiver operating characteristic (ROC) curves were constructed to validate classification performance results from the logistic regressions, which is quantified by the area under the curve (AUC). ROC curves were calculated for individual HCsf μ, ξ, and volume classifiers as well as combined 'μ and volume' and 'ξ and volume' classifiers. Statistical significance was determined at $\alpha = 0.05$.

2.6. Analysis 3: Interaction between HCsf MRE and volume measures in classifying aMCI

In addition to testing if HCsf MRE values add information about aMCI classification beyond HCsf volume, we wanted to determine whether MRE can identify aMCI in those who do not show signs of lower HCsf structural integrity from HCsf volume measures. We grouped participants based on HCsf volumes into low- and high-volume groups (split at the sample mean) and performed a stepwise logistic regression analysis, adjusting for age and sex. In these models, we added a volume group × HCsf MRE measure interaction to test if the contribution of the MRE measure differed between lower vs higher regional volumes (e.g., does DG-CA3 μ significantly differ in its classification of aMCI between 'low DG-CA3 volume' vs 'high DG-CA3 volume' groups?). Models were run only for significant HCsf MRE classifiers identified in analysis 2. Additionally, separate regression models, adjusted for age and sex, were fit to the data in each volume group to compare how HCsf μ was related to the predicted probability of aMCI in both the low- and high-volume groups. Statistical significance was determined at $\alpha = 0.05$.

3. Results

There were 6 total outliers in the μ data (HC: 1 CN; DG-CA3: 1 CN; SUB: 2 CN, 1 aMCI; ERC: 1 CN), 5 outliers in the ξ data (HC: 2 CN; DG-CA3: 2 CN, 1 aMCI; CA1-CA2: 2 CN; ERC: 1 CN), and 10 outliers in the volume data (DG-CA3: 2 CN, 3 aMCI; CA1-CA2: 2 CN, 2 aMCI; SUB: 2 CN, 1 aMCI; ERC: 1 CN). For each regional analysis, region-specific outliers were removed accordingly (ex. DG-CA3 μ outliers were removed in models involving DG-CA3 μ as a predictor). Table 1 below shows an overview of the participant demographics.

3.1. Analysis 1: Differential effects of aMCI on HCsf properties

In this analysis, we aimed to determine if significant HCsf MRE property differences existed between CN and aMCI older adults. Group means for each region and measure are shown in Table 2, including the p-values from the HC ANCOVA model and HCsf *post-hoc* pairwise group comparisons with Bonferroni correction from the LMM, as well as Cohen's *d* effect sizes for each model (Cohen, 1992). In both HC and HCsf, the aMCI group had lower μ, higher ξ, and smaller volumes, each of which indicated poorer structural integrity of those regions. Similar results for the MRE outcomes without normalization to global brain properties are presented in the Supplemental Information (Table S-2).

The HC ANCOVA results revealed that there were significant differences between CN and aMCI for HC volume [$F(1,79) = 11.3$, $p = 0.001$], while HC ξ was not significantly different [$F(1,77) = 2.05$, $p = 0.16$]. Levene's test of homogeneity was not significant for the HC volume and ξ models ($p > 0.3$) but was significant in the HC μ model ($p = 0.015$). To address this, the HC μ ANCOVA model was run with HC3 errors, which

Table 1
Overview of the participant demographics for CN and aMCI older adult groups. Total number of participants are displayed for each group as well as the sex distribution (male/female ratio) for each group. Average and standard deviation for age and NIH Toolbox (v. 2.1) composite score distributions (Weintraub et al., 2013) are shown for each group.

	CN	aMCI
Number	63	20
Sex (M/F)	19/44	5/15
Age (years)	69 ± 5.4	73 ± 8.7
NIH Toolbox Cognitive Battery: Total Composite Score	106.0 ± 9.0	95.4 ± 10.8
NIH Toolbox Cognitive Battery: Fluid Composite Score	96.0 ± 11.0	84.5 ± 13.9
NIH Toolbox Cognitive Battery: Crystallized Composite Score	115.9 ± 6.9	108.7 ± 7.4

Table 2
Summary of the normalized MRE and volume measures in CN and aMCI (mean ± standard deviation). P-values are results from the post-hoc pairwise comparisons with Bonferroni correction, adjusted for age and sex, and effect sizes for each comparison are presented as Cohen's *d*. * indicates significant group differences at $p < 0.05$.

Measure	Region	CN	aMCI	p-value	Cohen's *d*
Shear Stiffness, μ (kPa)	HC	2.84 ± 0.28	2.63 ± 0.32	**0.018***	**0.68**
	DG-CA3	3.04 ± 0.38	2.78 ± 0.52	**0.034***	**0.57**
	CA1-CA2	3.07 ± 0.28	2.84 ± 0.38	**0.007***	**0.68**
	SUB	2.73 ± 0.37	2.62 ± 0.33	0.272	0.32
	ERC	2.79 ± 0.37	2.71 ± 0.58	0.442	0.17
Damping Ratio, ξ	HC	0.204 ± 0.029	0.218 ± 0.037	0.156	0.41
	DG-CA3	0.224 ± 0.030	0.235 ± 0.030	0.189	0.35
	CA1-CA2	0.212 ± 0.025	0.230 ± 0.026	**0.025***	**0.70**
	SUB	0.174 ± 0.031	0.184 ± 0.036	0.284	0.30
	ERC	0.183 ± 0.033	0.181 ± 0.039	0.671	0.07
Volume (cm^3)	HC	7.65 ± 0.70	6.88 ± 0.80	**0.001***	**1.01**
	DG-CA3	1.57 ± 0.16	1.41 ± 0.20	**< 0.001***	**0.88**
	CA1-CA2	2.48 ± 0.28	2.18 ± 0.36	**< 0.001***	**0.93**
	SUB	0.89 ± 0.08	0.80 ± 0.10	**< 0.001***	**0.96**
	ERC	0.90 ± 0.10	0.82 ± 0.15	**0.028***	**0.62**

are robust to violations of assumptions. The HC μ model results showed there were significant group differences [$F(1,78) = 5.88$, $p = 0.018$]. Age and sex did not show significant group differences in HC μ and ξ models ($p > 0.05$), while age was significant in the HC volume model ($p < 0.001$).

The HCsf LMM μ model showed that there were significant group differences between CN and aMCI [$F(1,81.1) = 4.14$, $p = 0.045$]. Additionally, there was a significant group × HCsf interaction, which indicated the individual HCsf μ measures displayed differential effects in aMCI [$F(6,79) = 12.3$, $p < 0.001$]. Age and sex were not significant in the model ($p > 0.05$). *Post-hoc* pairwise comparisons with Bonferroni correction revealed only DG-CA3 μ ($p = 0.034$) and CA1-CA2 μ ($p = 0.007$) were significantly different between groups, while SUB μ and ERC μ did not show any significant group differences ($p > 0.2$) (Fig. 2).

The HCsf LMM ξ model did not display significant group differences [$F(1,78.9) = 1.23$, $p = 0.271$]. However, the group × HCsf interaction was significant [$F(6,79) = 68.5$, $p < 0.001$], indicating the HCsf ξ displayed significant differential effects in aMCI. Both age and sex were not significant in the model ($p > 0.05$). *Post-hoc* pairwise comparisons with Bonferroni correction showed only CA1-CA2 ξ displayed significant group differences ($p = 0.025$), while the other HCsf regions did not significantly differ between CN and aMCI (all $p > 0.1$) (Fig. 3).

For the HCsf LMM volume model, all HCsf regions displayed significant group differences between CN and aMCI [$F(1,70.8) = 20.2$, $p < 0.001$], while the group × HCsf interaction was also significant [$F(6,78.9) = 391.8$, $p < 0.001$]. Age was a significant factor in the model [$F(1,82.1) = 10.1$, $p = 0.002$], while sex was not [$F(1,74.4) = 3.93$, $p = 0.051$]. *Post-hoc* pairwise comparisons with Bonferroni correction revealed all regions displayed significant differences between CN and aMCI, with the strongest group differences in DG-CA3, CA1-CA2, and SUB volumes ($p < 0.001$), followed by ERC volume ($p = 0.028$) (Fig. 4).

3.2. Analysis 2: Contributions of HCsf MRE measures in classifying aMCI

We used logistic regression and ROC analyses to determine if the HC and HCsf regions with significant MRE measurement group differences (in Analysis 1) added information beyond regional volume in aMCI classification. Including stiffness measures significantly improved aMCI classification. The CA1-CA2 μ and CA1-CA2 volume combined analysis showed that the overall model was significant in classifying group differences [$\chi^2 = 22.1$, $p < 0.001$, Nagelkerke $R^2 = 0.370$]. CA1-CA2 volume was included as the first step ($p = 0.007$), followed by CA1-CA2 μ ($p = 0.010$), indicating that the stiffness measure added information for classifying aMCI beyond individual HCsf volume. This finding was further exemplified in an ROC analysis, which showed the combined CA1-CA2 μ and volume ROC curve had a larger AUC of 0.85 [95 % CI: 0.75–0.94], compared to the individual μ (AUC = 0.71 [95 % CI: 0.56–0.85]) and volume (AUC = 0.77 [95 % CI: 0.64–0.90]) ROC curves (Fig. 5A).

Similarly, the overall model combining both DG-CA3 μ and DG-CA3 volume significantly classified group differences [$\chi^2 = 19.9$, $p < 0.001$, Nagelkerke $R^2 = 0.349$]. DG-CA3 volume was included as the first step ($p = 0.002$), followed by DG-CA3 μ ($p = 0.026$). The combined DG-CA3 μ and volume ROC curve had a higher AUC of 0.83 [95 % CI:0.75–0.94], compared to the individual μ (AUC = 0.67 [95 % CI: 0.51–0.83]) and volume (AUC = 0.76 [95 % CI: 0.61–0.90]) ROC curves, further showcasing the value MRE adds to aMCI classification (Fig. 5B).

Considering the whole HC, the overall model combining both HC μ and HC volume significantly classified group differences [$\chi^2 = 21.4$, $p < 0.001$, Nagelkerke $R^2 = 0.342$]. HC volume was included as the first step ($p = 0.003$), followed by HC μ ($p = 0.020$). The combined HC μ and volume ROC curve had a higher AUC of 0.84 [95 % CI:0.75–0.93], compared to the individual μ (AUC = 0.72 [95 % CI: 0.57–0.86]) and volume (AUC = 0.76 [95 % CI: 0.63–0.88]) ROC curves.

While stiffness measures improved classification, stepwise regression analysis showed CA1-CA2 ξ did not significantly improve classification performance beyond CA1-CA2 volume ($p = 0.051$). Similar results for the MRE outcomes without normalization to global brain properties are presented in the Supplemental Information (Tables S-3 and S-4).

3.3. Analysis 3: Interaction between HCsf MRE and volume measures in classifying aMCI

Here, our goal was to expand on the results in Analysis 2 and show that even in the presence of high HCsf volumes, HCsf MRE metrics improve aMCI classification. After splitting the HCsf volume data into a low-volume group and high-volume group, the stepwise logistic regression analysis for DG-CA3 μ revealed a significant DG-CA3 volume group × DG-CA3 μ interaction ($p = 0.046$). Furthermore, lower DG-CA3 μ was significantly, linearly associated with a higher predicted probability for aMCI in the low DG-CA3 volume group [model $R^2 = 0.99$, $B = -0.11$, $p < 0.001$] (Fig. 6, purple line). These results show that at low DG-

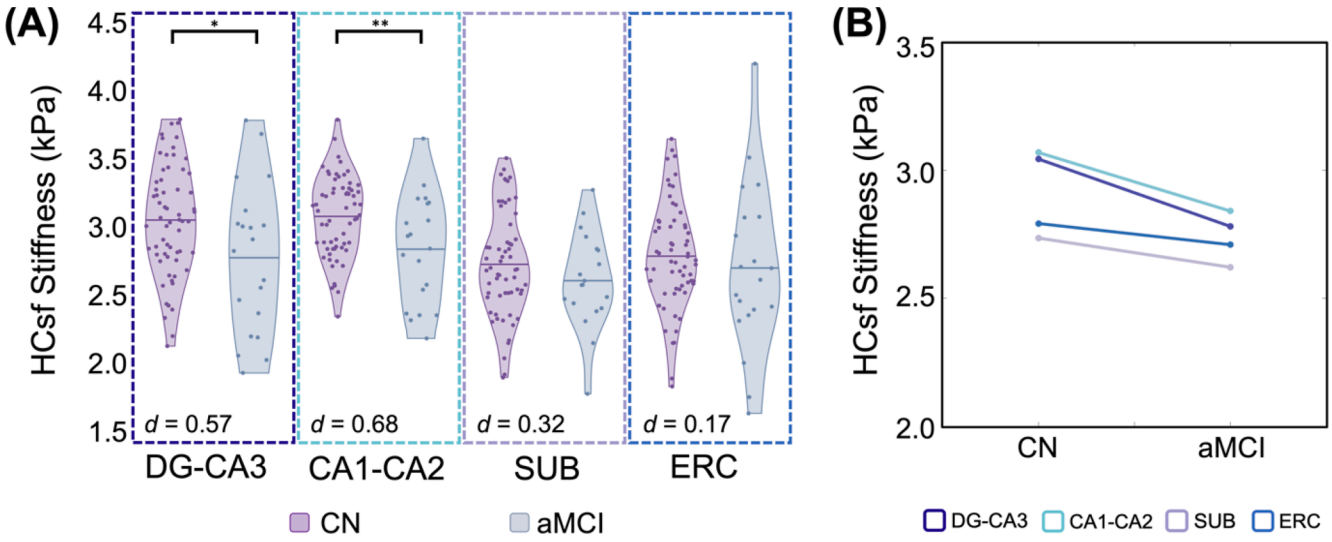

Fig. 2. HCsf μ differences between CN and aMCI groups. (A) Normalized HCsf μ plots showing significant differences in both the CA1-CA2 μ ($p = 0.007$) and DG-CA3 μ ($p = 0.034$) regions between groups. Cohen's *d* effect sizes for each region are shown on the plot, with medium effect sizes shown for the DG-CA3 and CA1-CA2 regions, while SUB displayed a small-medium effect size and ERC displayed a small effect size. *: $p < 0.05$; **: $p < 0.01$. (B) Illustration of significant group × HCsf interaction where group μ differences significantly varied between regions.

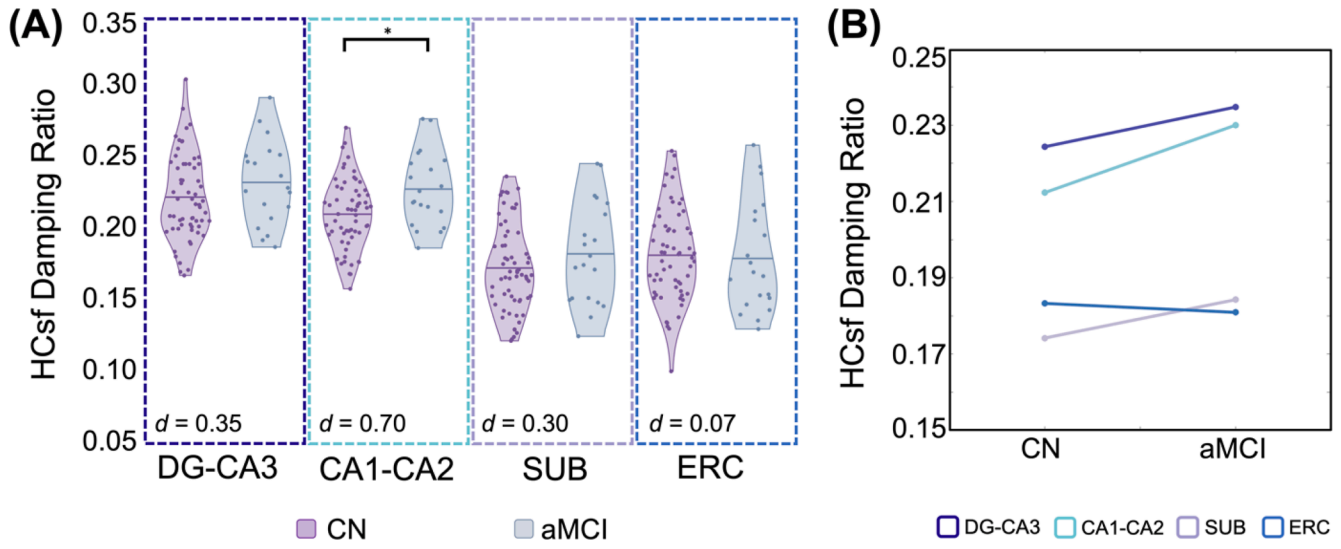

Fig. 3. HCsf ξ differences between CN and aMCI groups. (A) Normalized HCsf ξ plots showing significant differences in CA1-CA2 ξ ($p = 0.025$) between groups. Cohen's *d* effect sizes for each region are shown on the plot, with a medium-large effect size shown for CA1-CA2, while the other HCsf regions displayed small-medium effect sizes. *: $p < 0.05$. (B) Illustration of significant group × HCsf interaction where group ξ differences significantly varied between regions.

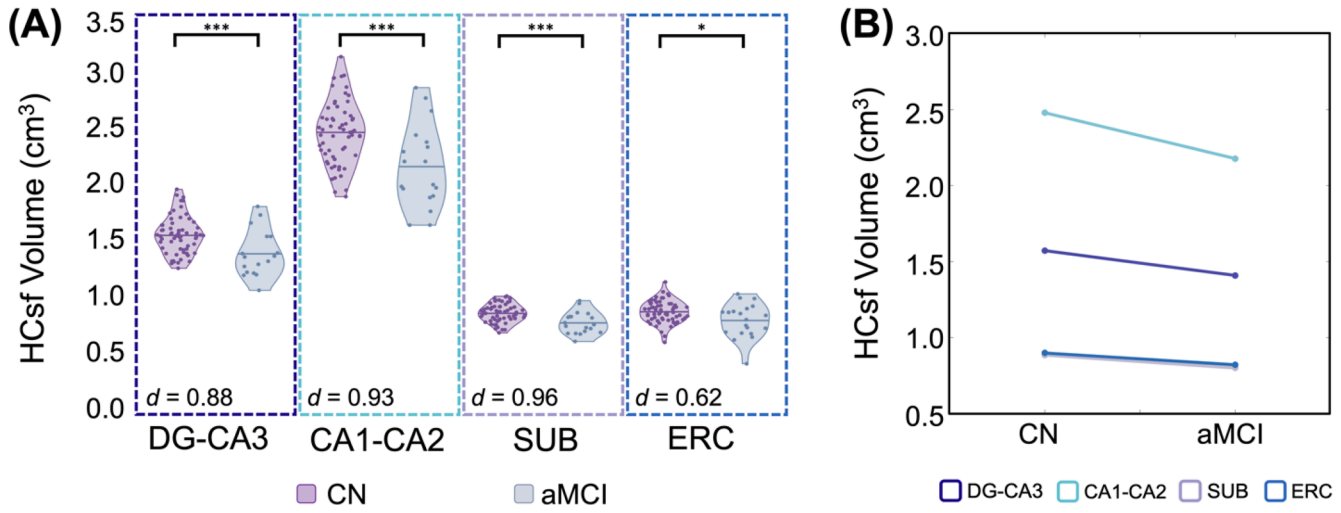

Fig. 4. HCsf volume differences between CN and aMCI groups. (A) Normalized HCsf volume plots showing significant differences in all HCsf ($p < 0.05$) between groups. Cohen's *d* effect sizes for each region are shown on the plot, with large effect sizes shown for DG-CA3, CA1-CA2, and SUB, while ERC displayed a medium effect size. *: $p < 0.05$; ***: $p < 0.001$. (B) Illustration of significant group × HCsf interaction where group volume differences significantly varied between regions.

CA3 volumes, low μ values can predict aMCI diagnosis. In the high DG-CA3 volume group, a quadratic regression found that lower DG-CA3 μ was significantly, nonlinearly associated with a higher predicted probability of aMCI classification [model $R^2 = 0.99$, (DG-CA3 μ: B = -2.94, $p < 0.001$); (DG-CA3 μ^2: B = 0.43, $p < 0.001$)] (Fig. 6, turquoise line). This signifies that despite high DG-CA3 volumes, the likelihood of an aMCI diagnosis is much higher with lower DG-CA3 μ, and further exemplifies the value of the information added by MRE compared to volume. The CA1-CA2 volume group × CA1-CA2 MRE interaction term for both CA1-CA2 μ and ξ models were not significant in their respective models ($p > 0.2$). Similar results for the MRE outcomes without normalization to global brain properties are presented in the Supplemental Information (Table S-5).

4. Discussion

In this work, we sought to evaluate the value of using MRE to assess HCsf viscoelastic property differences between older adults with and without aMCI. We showed that HCsf MRE measures add value in assessing differences between cognitively normal (CN) and aMCI participants, even beyond established HCsf volume measures. There were significant group differences observed in HC μ, which aligns with prior MRE work related to the decline in brain viscoelasticity in both aging in older adults (Arani et al., 2015; Hiscox et al., 2018; Sack et al., 2011) and neurodegeneration (Gerischer et al., 2018; Hiscox et al., 2020a; Murphy et al., 2011, 2016), as well as in individual HCsf regions, consistent with the expectation that differences in tissue viscoelasticity measured with MRE will be in regions primarily affected by AD pathology (Gerischer et al., 2018; Hiscox et al., 2020a; Murphy et al., 2016). Pathological hallmarks such as neurofibrillary tangle (NFT) and amyloid-beta plaque accumulation often occurs in the hippocampus and its subregions during aMCI and future progression of AD (Braak and Braak, 1991; Lace et al., 2009). Stiffness, μ, is thought to reflect tissue composition, while damping ratio, ξ, is thought to reflect tissue organization (Hiscox et al., 2021, 2016; Sack et al., 2013), both of which may reflect changes to the underlying tissue microstructure in aMCI. While properties of the whole

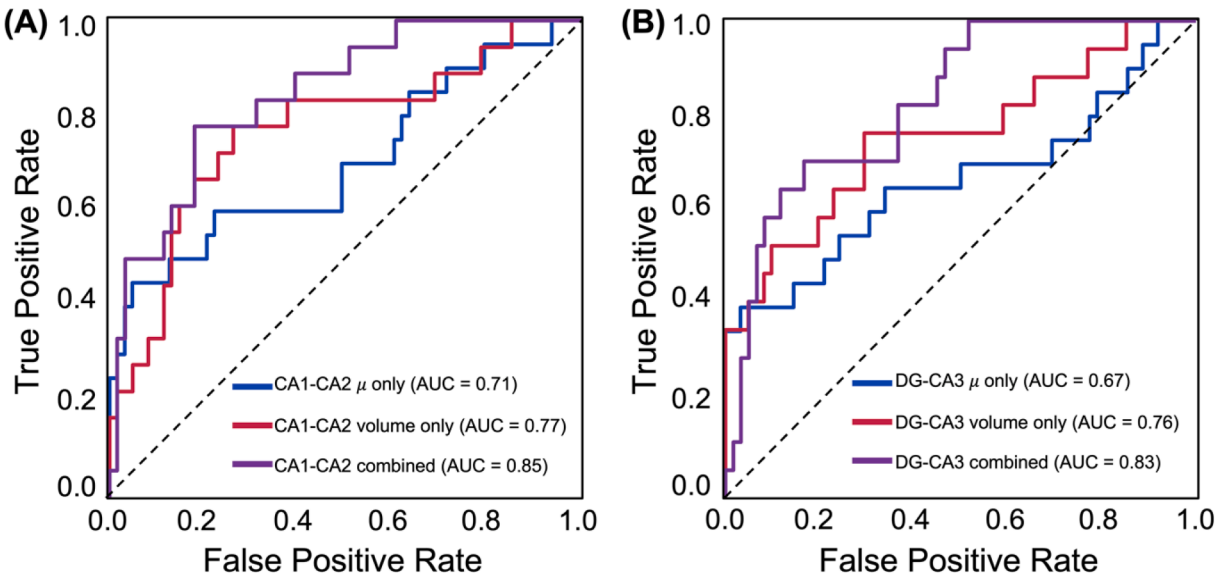

Fig. 5. Receiver operating characteristic (ROC) curves for significant HCsf predictors in classifying group differences between CN and aMCI, with area under the curve (AUC) included as a measure of predictive performance. (A) CA1-CA2 ROC curves: CA1-CA2 μ, CA1-CA2 volume, and combined CA1-CA2 μ and volume predictors from the logistic regression, with the combined ROC curve performing the best of the three (AUC = 0.85). (B) DG-CA3 ROC curves: DG-CA3 μ, DG-CA3 volume, and combined DG-CA3 μ and volume predictors from the logistic regression, with the combined ROC curve performing the best of the three (AUC = 0.83).

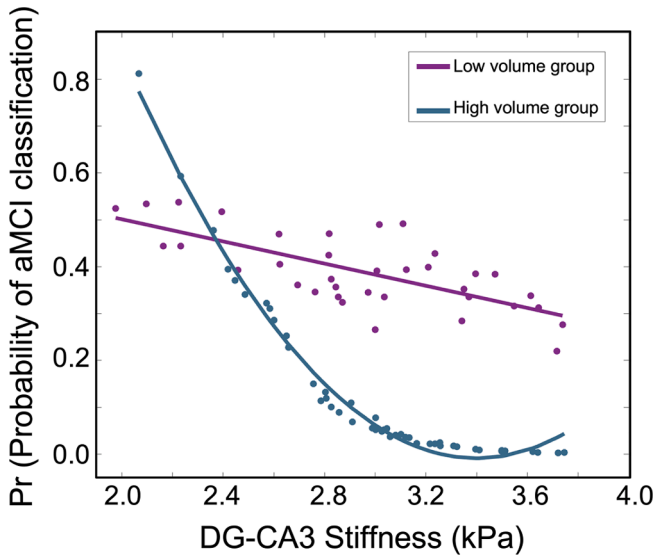

Fig. 6. Overview of the relationship between predicted probability of aMCI classification and DG-CA3 μ for both the low-volume group (purple line) and high-volume group (turquoise line). Both groups show that higher predicted probabilities significantly associated with lower DG-CA3 μ for both groups. The low volume group displayed a significant, linear relationship between predicted probability of aMCI (Pr-aMCI) and DG-CA3 μ (B = -0.11, $p < 0.001$), while the high volume group displayed a significant non-linear relationship between Pr-aMCI and DG-CA3 μ ([DG-CA3 μ: B = -2.94, $p < 0.001$]; [DG-CA3 μ^2: B = 0.43, $p < 0.001$]).

HC are different between groups, examining individual HCsf may provide metrics related to the spatial distribution of pathological changes to tissue microstructure.

Both μ and ξ of the CA1-CA2 region were significantly different between groups, with aMCI exhibiting lower stiffness and higher damping ratio, both indicative of poorer tissue integrity. This finding agrees with our initial hypothesis, as several studies have cited significant structural changes in the CA1-CA2 region in aMCI and AD before the other subfields (Chételat et al., 2008; de Flores et al., 2015; La Joie et al., 2013; Mueller et al., 2010; Mueller and Weiner, 2009). Other studies cite similar structural and functional changes in this region, with one longitudinal study finding a reduction in functional connectivity in both the right CA1 and left CA2 regions in aMCI (Li et al., 2018), while another study found that amyloid positive individuals with aMCI exhibited greater shape deformation in the CA1 region (Ye et al., 2014). These findings point to further microstructural degradation in this region, which aligns with our observation of lower CA1-CA2 stiffness. Furthermore, the CA1-CA2 region contains pyramidal cells that have a diffusive branch-like organization that may be disrupted in neurodegeneration (Duvernoy, 2005). In the progression of AD, the accumulation of the NFTs in this region could potentially cause the dendritic organization to breakdown (Braak and Braak, 1991), leading to more energy dissipation in this region in aMCI, which could explain the greater CA1-CA2 damping ratio, indicating more viscous tissue behavior. Recent works have sought to examine the effects of amyloid-beta protein on MRE measures, and found it may cause higher damping ratio with minimal to no effect on stiffness (Bigot et al., 2020; Palotai et al., 2022), which is a potential mechanism for the greater CA1-CA2 damping ratio observed here in aMCI patients.

We also found significant group differences in DG-CA3 μ, with aMCI exhibiting lower stiffness. Some imaging studies observed significant volumetric decline in the DG region in the course of AD (Pluta et al., 2012; Yassa et al., 2010) and large shape deformations in this region in aMCI (Yassa et al., 2010). This may cause disruption in the tightly organized granule cells and its unmyelinated mossy fibers of the DG-CA3 (Duvernoy, 2005). One *in vivo* study looked at subfield diffusion neurite orientation dispersion and density imaging (NODDI) metrics and found the DG region was significantly affected in MCI individuals compared to healthy controls. Furthermore, associations between DG microstructural changes and an increase in the AD-related neurofilament light biomarker, which is a measure of axonal damage, may lead to structural changes observed in this region (Shahid et al., 2022), which aligns with our findings. In this study, we did not find significant group differences in SUB or ERC in either MRE measure. On the AD spectrum, all HCsf regions are ultimately affected and experience structural degeneration (de Flores et al., 2015), but as aMCI is an early stage of disease progression, these regions may be on a different time course compared to CA1-CA2 and DG-CA3. Longitudinal progression to the later stages of AD may result in significant structural decline in SUB and ERC, as quantified

by significant changes in MRE measures.

MRE studies focusing on brain tissue viscoelasticity in AD showed that the brain appears softer on average (Murphy et al., 2011), with the most pronounced effects in frontal, parietal, and temporal lobes (Murphy et al., 2016), specific cortical regions (Hiscox et al., 2020a), and the HC (Gerischer et al., 2018) – all of which are particularly affected in AD. Prior MRE animal work has attributed tissue softening to neuronal loss (Freimann et al., 2013) and demyelination (Schregel et al., 2012), which shows that brain stiffness may reflect composition changes in the tissue during disease progression. In corresponding MRE studies on animal models, tissue softening occurred in animals with AD (Majumdar and Klatt, 2021; Murphy et al., 2012), further supporting the results presented in this study. To date, the sole MRE study that investigated MCI effects on tissue viscoelasticity showed no significant changes between MCI and cognitively normal individuals (Murphy et al., 2016); however, the small sample size could explain the failure to find significant differences between groups. Overall, our results complement prior MRE work on AD patients, where we show similarly lower tissue stiffness but in an earlier stage of the disease. Furthermore, these findings show our high-resolution MRE protocol can capture the effects of aMCI on individual HCsf viscoelasticity, which are regions that are expected to differentially experience pathology at this disease stage.

The second portion of this study focused on evaluating MRE as a useful metric in classifying aMCI beyond volume. Both CA1-CA2 μ and DG-CA3 μ improved aMCI classification beyond the CA1-CA2 and DG-CA3 volume measures. Prior MRE work in neurological diseases show the benefit of combining volume and MRE metrics to improve classification (Gerischer et al., 2018; Huesmann et al., 2020). Specifically, when adding HC stiffness to diffusion and volume MRI metrics, there was a significant improvement in the accuracy of AD diagnosis (Gerischer et al., 2018). This indicates that regional MRE measures are not overly biased by differences in regional volume between individuals, which is consistent with prior MRE work that showed MRE measures were significantly different in AD patients even when controlling for volume (Hiscox et al., 2020a), while cognitive measures were not correlated with volume but were associated with MRE metrics (Hiscox et al., 2020b; Johnson et al., 2018; Schwarb et al., 2016). Instead MRE measures add unique information beyond volumetrics indicating additional value in detecting aMCI and potentially early detection of AD. This is further exemplified by our finding that low DG-CA3 μ is associated with a higher probability of aMCI diagnosis regardless of DG-CA3 volume atrophy measures. There is a non-linear relationship between aMCI and DG-CA3 μ in the high-volume group, such that individuals with high volume and high stiffness are not likely to have aMCI, though that probability becomes significantly greater with lower stiffness – even if there is still high volume.

The findings in this work hint that MRE and volumetric measures of HCsf structures may detect structural integrity with different underlying mechanisms. Volume is a measure of regional structural decline and atrophy (Mueller et al., 2010), while MRE viscoelastic measures are thought to reflect tissue organization and composition changes, which may occur in neurodegeneration prior to measurable tissue atrophy (Murphy et al., 2019). aMCI leads to atrophy in the HCsf due to neuronal cell breakdown (Khan et al., 2015), which can ultimately lead to a decline in the size of all HCsf regions. However, since MRE metrics reflect cellular and matrix organization and composition through mechanical properties, that may occur without or before atrophy of the HCsf. This may explain why we see strong differences in tissue stiffness between CN and aMCI in isolated regions of the HCsf even in the absence of volumetric differences, which could be due to early stages of pathology. Previous MRE studies have cited brain tissue stiffness decline reflecting microstructural events such as altered synaptic connectivity, cytoskeletal architectural breakdown, and extracellular matrix degeneration (Hiscox et al., 2020a; Huston et al., 2016; Murphy et al., 2019, 2011). This is further supported in studies that found changes in synaptic dysfunction (Scheff et al., 2007; Scheff et al., 2006) and mechanical signaling changes (Hall et al., 2021) in the HC and its subfield regions in neurodegeneration. In all, these structural changes may lead to a decrease in the viscoelastic behavior of tissue that may not be reflected in volumetric atrophy.

This study has several limitations. The current work is based on a cross-sectional analysis while a longitudinal analysis may provide more insight into the how HCsf viscoelastic properties change differently with age and in relation to volume changes with aMCI and further AD progression. Longitudinal studies may also allow the analysis of HCsf viscoelasticity in participants who develop aMCI and those who convert from aMCI to dementia status. Prior work found that participants who converted from aMCI to dementia experienced structural decline in the CA1 region before the other subfields (Chételat et al., 2008). Furthermore, no apolipoprotein E carrier status or positron emission tomography (PET) imaging data for amyloid and tau were collected. Inclusion of these data in future work may provide more insight into the specific HCsf viscoelastic changes we observed in this study. We also did not have complementary histopathological studies to understand the specific cellular pathology that is occurring in these regions and its relation to MRE metrics. These studies should be considered in future work.

5. Conclusion

The goal of this study was to evaluate group differences between CN and aMCI using HCsf MRE viscoelastic property measures. We showed that we can detect group differences in both μ and ξ in individual HCsf, indicating reduced tissue integrity in aMCI. We also found that combining both HCsf MRE and volume measures improved group classification, showcasing the value of HCsf metrics in identifying differences in health and disease, and that MRE metrics are still predictive of aMCI even when HCsf volume is high, suggesting a potential for early of disease. Overall, this work established HCsf MRE metrics as potential clinical imaging biomarkers for detecting structural decline in neurodegenerative diseases. Future work will involve longitudinal studies to understand how HCsf MRE properties may change throughout AD progression.

CRediT authorship contribution statement

Peyton L. Delgorio: Conceptualization, Investigation, Data curation, Formal analysis, Writing – original draft. **Lucy V. Hiscox:** Investigation, Data curation, Writing – review & editing. **Grace McIlvain:** Investigation, Data curation, Writing – review & editing. **Mary K. Kramer:** Investigation, Data curation, Writing – review & editing. **Alexa M. Diano:** Investigation, Data curation, Writing – review & editing. **Kyra E. Twohy:** Investigation, Data curation, Writing – review & editing. **Alexis A. Merritt:** Data curation, Writing – review & editing, Project administration. **Matthew D.J. McGarry:** Methodology, Resources, Writing – review & editing. **Hillary Schwarb:** Conceptualization, Writing – review & editing. **Ana M. Daugherty:** Conceptualization, Writing – review & editing. **James M. Ellison:** Conceptualization, Writing – review & editing. **Alyssa M. Lanzi:** Resources, Writing – review & editing. **Matthew L. Cohen:** Resources, Writing – review & editing. **Christopher R. Martens:** Conceptualization, Resources, Writing – review & editing, Funding acquisition. **Curtis L. Johnson:** Conceptualization, Methodology, Resources, Writing – review & editing, Supervision, Funding acquisition.

Declaration of Competing Interest

The authors declare that they have no known competing financial interests or personal relationships that could have appeared to influence the work reported in this paper.

Data availability

Data will be made available on request.

Acknowledgements

This research was supported by grants from the National Institutes of Health: R01-AG058853, R01-EB027577, and K01-AG054731. Participant recruitment was organized through the Delaware Center for Cognitive Aging Research.

Appendix A. Supplementary data

Supplementary data to this article can be found online at https://doi.org/10.1016/j.nicl.2023.103327.

References

Albert, M.S., DeKosky, S.T., Dickson, D., Dubois, B., Feldman, H.H., Fox, N.C., Gamst, A., Holtzman, D.M., Jagust, W.J., Petersen, R.C., Snyder, P.J., Carrillo, M.C., Thies, B., Phelps, C.H., 2011. The diagnosis of mild cognitive impairment due to Alzheimer's disease: Recommendations from the National Institute on Aging-Alzheimer's Association workgroups on diagnostic guidelines for Alzheimer's disease. Alzheimer's Dement. 7, 270–279. https://doi.org/10.1016/j.jalz.2011.03.008.

Arani, A., Murphy, M.C., Glaser, K.J., Manduca, A., Lake, D.S., Kruse, S.A., Jack, C.R., Ehman, R.L., Huston, J., 2015. Measuring the effects of aging and sex on regional brain stiffness with MR elastography in healthy older adults. Neuroimage 111, 59–64.

Benedict, R.H.B., Schretlen, D., Groninger, L., Brandt, J., 1998. Hopkins verbal learning test - Revised: Normative data and analysis of inter-form and test-retest reliability. Clin. Neuropsychol. 12, 43–55. https://doi.org/10.1076/clin.12.1.43.1726.

Bigot, M., Chauveau, F., Amaz, C., Sinkus, R., Beuf, O., Lambert, S.A., 2020. The apparent mechanical effect of isolated amyloid-β and α-synuclein aggregates revealed by multi-frequency MRE. NMR Biomed. 33, e4174.

Braak, H., Braak, E., 1991. Neuropathological stageing of Alzheimer-related changes. Acta Neuropathol 82 (4), 239–259.

Breijyeh, Z., Karaman, R., 2020. Comprehensive Review on Alzheimer's Disease: Causes and Treatment. Molecules 25, 5789.

Chételat, G., Fouquet, M., Kalpouzos, G., Denghien, I., De la Sayette, V., Viader, F., Mézenge, F., Landeau, B., Baron, J.C., Eustache, F., Desgranges, B., 2008. Three-dimensional surface mapping of hippocampal atrophy progression from MCI to AD and over normal aging as assessed using voxel-based morphometry. Neuropsychologia 46, 1721–1731. https://doi.org/10.1016/j.neuropsychologia.2007.11.037.

Cohen, J., 1992. Quantitative methods in psychology: A power primer. Psychological Bulletin 112 (1), 155–159.

Cook, S.E., Marsiske, M., McCoy, K.J.M., 2009. The use of the modified telephone interview for cognitive status (Tics-M) in the detection of amnestic mild cognitive impairment. J. Geriatr. Psychiatry Neurol. 22, 103–109. https://doi.org/10.1177/0891988708328214.

de Flores, R., La Joie, R., Chételat, G., 2015. Structural imaging of hippocampal subfields in healthy aging and Alzheimer's disease. Neuroscience 309, 29–50. https://doi.org/10.1016/j.neuroscience.2015.08.033.

Delgorio, P.L., Hiscox, L.V., Daugherty, A.M., Sanjana, F., Pohlig, R.T., Ellison, J.M., Martens, C.R., Schwarb, H., McGarry, M.D.J., Johnson, C.L., 2021. Effect of Aging on the Viscoelastic Properties of Hippocampal Subfields Assessed with High-Resolution MR Elastography. Cereb. Cortex 31, 2799–2811. https://doi.org/10.1093/cercor/bhaa388.

Delgorio, P.L., Hiscox, L.V., Daugherty, A.M., Sanjana, F., McIlvain, G., Pohlig, R.T., McGarry, M.D.J., Martens, C.R., Schwarb, H., Johnson, C.L., 2022. Structure-Function Dissociations of Human Hippocampal Subfield Stiffness and Memory Performance. J. Neurosci. 42, 7957–7968. https://doi.org/10.1523/JNEUROSCI.0592-22.2022.

Du, A.T., Schuff, N., Amend, D., Laakso, M.P., Hsu, Y.Y., Jagust, W.J., Yaffe, K., Kramer, J.H., Reed, B., Norman, D., Chui, H.C., Weiner, M.W., 2001. Magnetic resonance imaging of the entorhinal cortex and hippocampus in mild cognitive impairment and Alzheimer's disease. J. Neurol. Neurosurg. Psychiatry 71, 441–447. https://doi.org/10.1136/jnnp.71.4.441.

Du, A.-T., Schuff, N., Chao, L.L., Kornak, J., Jagust, W.J., Kramer, J.H., Reed, B.R., Miller, B.L., Norman, D., Chui, H.C., Weiner, M.W., 2006. Age effects on atrophy rates of entorhinal cortex and hippocampus. Neurobiol. Aging 27 (5), 733–740.

Duvernoy, H.M., 2005. The human hippocampus: functional anatomy, vascularization and serial sections with MRI. Springer Science & Business Media.

Fischl, B., 2012. FreeSurfer. Neuroimage 62 (2), 774–781.

Folstein, M.F., Lee, R., Helzer, J.E., 1983. The mini-mental state examination. Arch Gen Psychiatry 7, 812.

Freimann, F.B., Müller, S., Streitberger, K.J., Guo, J., Rot, S., Ghori, A., Vajkoczy, P., Reiter, R., Sack, I., Braun, J., 2013. MR elastography in a murine stroke model reveals correlation of macroscopic viscoelastic properties of the brain with neuronal density. NMR Biomed. 26, 1534–1539. https://doi.org/10.1002/nbm.2987.

Gauthier, S., Reisberg, B., Zaudig, M., Petersen, R.C., Ritchie, K., Broich, K., Belleville, S., Brodaty, H., Bennett, D., Chertkow, H., Cummings, J.L., de Leon, M., Feldman, H., Ganguli, M., Hampel, H., Scheltens, P., Tierney, M.C., Whitehouse, P., Winblad, B., 2006. Mild cognitive impairment. Lancet 367, 1262–1270. https://doi.org/10.1016/S0140-6736(06)68542-5.

Gerischer, L.M., Fehlner, A., Köbe, T., Prehn, K., Antonenko, D., Grittner, U., Braun, J., Sack, I., Flöel, A., 2018. Combining viscoelasticity, diffusivity and volume of the hippocampus for the diagnosis of Alzheimer's disease based on magnetic resonance imaging. NeuroImage Clin. 18, 485–493. https://doi.org/10.1016/j.nicl.2017.12.023.

Hall, C.M., Moeendarbary, E., Sheridan, G.K., 2021. Mechanobiology of the brain in ageing and Alzheimer's disease. Eur. J. Neurosci. 53, 3851–3878. https://doi.org/10.1111/ejn.14766.

Hannum, A.J., McIlvain, G., Sowinski, D., McGarry, M.D.J., Johnson, C.L., 2022. Correlated Noise in Brain Magnetic Resonance Elastography. Magn. Reson. Med. 87, 1313–1328. https://doi.org/10.1002/mrm.29050.

Hiscox, L.V., Johnson, C.L., Barnhill, E., McGarry, M.D.J., Huston, J., van Beek, E.J.R., Starr, J.M., Roberts, N., 2016. Magnetic resonance elastography (MRE) of the human brain: Technique, findings and clinical applications. Phys. Med. Biol. 61 (24), R401–R437.

Hiscox, L.V., Johnson, C.L., McGarry, M.D.J., Perrins, M., Littlejohn, A., van Beek, E.J.R., Roberts, N., Starr, J.M., 2018. High-resolution magnetic resonance elastography reveals differences in subcortical gray matter viscoelasticity between young and healthy older adults. Neurobiol. Aging 65, 158–167. https://doi.org/10.1016/j.neurobiolaging.2018.01.010.

Hiscox, L.V., Johnson, C.L., McGarry, M.D.J., Marshall, H., Ritchie, C.W., Beek, E.J.R.V., Roberts, N., Starr, J.M., 2020a. Mechanical property alterations across the cerebral cortex due to Alzheimer's disease. Brain Commun. 2, fcz049. https://doi.org/10.1093/braincomms/fcz049.

Hiscox, L.V., Johnson, C.L., McGarry, M.D.J., Schwarb, H., van Beek, E.J.R., Roberts, N., Starr, J.M., 2020b. Hippocampal viscoelasticity and episodic memory performance in healthy older adults examined with magnetic resonance elastography. Brain Imaging Behav. 14, 175–185. https://doi.org/10.1007/s11682-018-9988-8.

Hiscox, L.V., Schwarb, H., McGarry, M.D.J., Johnson, C.L., 2021. Aging brain mechanics: Progress and promise of magnetic resonance elastography. Neuroimage 232, 117889. https://doi.org/10.1016/j.neuroimage.2021.117889.

Huesmann, G.R., Schwarb, H., Smith, D.R., Pohlig, R.T., Anderson, A.T., McGarry, M.D.J., Paulsen, K.D., Wszalek, T.M., Sutton, B.P., Johnson, C.L., 2020. Hippocampal stiffness in mesial temporal lobe epilepsy measured with MR elastography: Preliminary comparison with healthy participants. NeuroImage Clin. 27, 102313 https://doi.org/10.1016/j.nicl.2020.102313.

Huston, J., Murphy, M.C., Boeve, B.F., Fattahi, N., Arani, A., Glaser, K.J., Manduca, A., Jones, D.T., Ehman, R.L., 2016. Magnetic resonance elastography of frontotemporal dementia. J. Magn. Reson. Imaging 43 (2), 474–478.

Jack, C.R., Twomey, C.K., Zinsmeister, A.R., Sharbrough, F.W., Petersen, R.C., Cascino, G.D., 1989. Anterior temporal lobes and hippocampal formations: normative volumetric measurements from MR images in young adults. Radiology 172 (2), 549–554.

Jenkinson, M., Bannister, P.R., Brady, M., Smith, S.M., 2002. Improved Optimization for the Robust and Accurate Linear Registration and Motion Correction of Brain Images. Neuroimage 17, 825–841. https://doi.org/10.1006/nimg.2002.1132.

Jenkinson, M., Beckmann, C.F., Behrens, T.E.J., Woolrich, M.W., Smith, S.M., 2012. FSL. Neuroimage 62 (2), 782–790.

Johnson, C.L., Holtrop, J.L., Anderson, A.T., Sutton, B.P., 2016a. Brain MR elastography with multiband excitation and nonlinear motion-induced phase error correction. Proc. Intl. Soc. Mag. Res. Med. 1951.

Johnson, C.L., Schwarb, H., McGarry, M.D.J., Anderson, A.T., Huesmann, G.R., Sutton, B.P., Cohen, N.J., 2016b. Viscoelasticity of subcortical gray matter structures. Hum. Brain Mapp. 37, 4221–4233. https://doi.org/10.1002/hbm.23314.

Johnson, C.L., Schwarb, H., Horecka, K.M., McGarry, M.D.J., Hillman, C.H., Kramer, A.F., Cohen, N.J., Barbey, A.K., 2018. Double dissociation of structure-function relationships in memory and fluid intelligence observed with magnetic resonance elastography. Neuroimage 171, 99–106. https://doi.org/10.1016/j.neuroimage.2018.01.007.

Kerchner, G.A., Berdnik, D., Shen, J.C., Bernstein, J.D., Fenesy, M.C., Deutsch, G.K., Wyss-Coray, T., Rutt, B.K., 2014. APOE ε4 worsens hippocampal CA1 apical neuropil atrophy and episodic memory. Neurology 82, 691–697.

Khan, W., Westman, E., Jones, N., Wahlund, L.-O., Mecocci, P., Vellas, B., Tsolaki, M., Kłoszewska, I., Soininen, H., Spenger, C., Lovestone, S., Muehlboeck, J.-S., Simmons, A., 2015. Automated Hippocampal Subfield Measures as Predictors of Conversion from Mild Cognitive Impairment to Alzheimer's Disease in Two Independent Cohorts. Brain Topogr. 28 (5), 746–759.

Klein, C., Hain, E.G., Braun, J., Riek, K., Mueller, S., Steiner, B., Sack, I., Paul, F., 2014. Enhanced adult neurogenesis increases brain stiffness: In vivo magnetic resonance elastography in a mouse model of dopamine depletion. PLoS One 9 (3). https://doi.org/10.1371/journal.pone.0092582.

La Joie, R., Perrotin, A., De La Sayette, V., Egret, S., Doeuvre, L., Belliard, S., Eustache, F., Desgranges, B., Chételat, G., 2013. Hippocampal subfield volumetry in mild cognitive impairment, Alzheimer's disease and semantic dementia. NeuroImage Clin. 3, 155–162. https://doi.org/10.1016/j.nicl.2013.08.007.

Lace, G., Savva, G.M., Forster, G., De Silva, R., Brayne, C., Matthews, F.E., Barclay, J.J., Dakin, L., Ince, P.G., Wharton, S.B., 2009. Hippocampal tau pathology is related to neuroanatomical connections: An ageing population-based study. Brain 132, 1324–1334. https://doi.org/10.1093/brain/awp059.

Lavenex, P., Lavenex, P.B., 2013. Building hippocampal circuits to learn and remember: insights into the development of human memory. Behav. Brain Res. 254, 8–21.

Li, H., Jia, X., Qi, Z., Fan, X., Ma, T., Pang, R., Ni, H., Li, C., shan, R., Lu, J., Li, K., 2018. Disrupted functional connectivity of cornu ammonis subregions in amnestic mild cognitive impairment: A longitudinal resting-state fMRI study. Front. Hum. Neurosci. 12, 413. https://doi.org/10.3389/fnhum.2018.00413.

Lilliefors, H.W., 1967. On the Kolmogorov-Smirnov test for normality with mean and variance unknown. J. Am. Stat. Assoc. 62 (318), 399–402.

Majumdar, S., Klatt, D., 2021. Longitudinal study of sub-regional cerebral viscoelastic properties of 5XFAD Alzheimer's disease mice using multifrequency MR elastography. Magn. Reson. Med. 86, 405–414. https://doi.org/10.1002/mrm.28709.

McGarry, M.D.J., Van Houten, E.E.W., Perrïez, P.R., Pattison, A.J., Weaver, J.B., Paulsen, K.D., 2011. An octahedral shear strain-based measure of SNR for 3D MR elastography. Phys. Med. Biol. 56, N153–N164. https://doi.org/10.1088/0031-9155/56/13/N02.

McGarry, M.D.J., Van Houten, E.E.W., Johnson, C.L., Georgiadis, J.G., Sutton, B.P., Weaver, J.B., Paulsen, K.D., 2012. Multiresolution MR elastography using nonlinear inversion. Med. Phys. 39, 6388–6396. https://doi.org/10.1118/1.4754649.

McGarry, M.D.J., Johnson, C.L., Sutton, B.P., Van Houten, E.E., Georgiadis, J.G., Weaver, J.B., Paulsen, K.D., 2013. Including spatial information in nonlinear inversion MR elastography using soft prior regularization. IEEE Trans. Med. Imaging 32, 1901–1909. https://doi.org/10.1109/TMI.2013.2268978.

McIlvain, G., Cerjanic, A.M., Christodoulou, A.G., McGarry, M.D.J., Johnson, C.L., 2022a. OSCILLATE: A low-rank approach for accelerated magnetic resonance elastography. Magn. Reson. Med. 88, 1659–1672. https://doi.org/10.1002/mrm.29308.

McIlvain, G., McGarry, M.D.J., Johnson, C.L., 2022b. Quantitative Effects of Off-Resonance Related Distortion on Brain Mechanical Property Estimation with Magnetic Resonance Elastography. NMR Biomed. 35, e4616.

Moise, P., Schwarzinger, M., Um, M.-Y., 2004. Dementia care in 9 OECD countries: a comparative analysis. Doi: 10.1787/485700737071.

Morris, J.C., 1993. The Clinical Dementia Rating (CDR): current version and scoring rules. Neurology 43 (11).

Mueller, S.G., Schuff, N., Yaffe, K., Madison, C., Miller, B., Weiner, M.W., 2010. Hippocampal atrophy patterns in mild cognitive impairment and alzheimer's disease. Hum. Brain Mapp. 31, 1339–1347. https://doi.org/10.1002/hbm.20934.

Mueller, S.G., Weiner, M.W., 2009. Selective effect of age, Apo e4, and Alzheimer's disease on hippocampal subfields. Hippocampus 19, 558–564. https://doi.org/10.1002/hipo.20614.

Murphy, M.C., Huston, J., Jack, C.R., Glaser, K.J., Manduca, A., Felmlee, J.P., Ehman, R. L., 2011. Decreased brain stiffness in Alzheimer's disease determined by magnetic resonance elastography. J. Magn. Reson. Imaging 34 (3), 494–498.

Murphy, M.C., Curran, G.L., Glaser, K.J., Rossman, P.J., Huston, J., Poduslo, J.F., Jack, C. R., Felmlee, J.P., Ehman, R.L., 2012. Magnetic resonance elastography of the brain in a mouse model of Alzheimer's disease: Initial results. Magn. Reson. Imaging 30 (4), 535–539.

Murphy, M.C., Huston, J., Glaser, K.J., Manduca, A., Meyer, F.B., Lanzino, G., Morris, J. M., Felmlee, J.P., Ehman, R.L., 2013. Preoperative assessment of meningioma stiffness using magnetic resonance elastography. J. Neurosurg. 118, 643–648. https://doi.org/10.3171/2012.9.JNS12519.

Murphy, M.C., Jones, D.T., Jack, C.R., Glaser, K.J., Senjem, M.L., Manduca, A., Felmlee, J.P., Carter, R.E., Ehman, R.L., Huston, J., 2016. Regional brain stiffness changes across the Alzheimer's disease spectrum. NeuroImage Clin. 10, 283–290.

Murphy, M.C., Huston, J., Ehman, R.L., 2019. MR elastography of the brain and its application in neurological diseases. Neuroimage 187, 176–183. https://doi.org/10.1016/j.neuroimage.2017.10.008.

Palotai, M., Schregel, K., Nazari, N., Merchant, J.P., Taylor, W.M., Guttmann, C.R.G., Sinkus, R., Young-Pearse, T.L., Patz, S., 2022. Magnetic resonance elastography to study the effect of amyloid plaque accumulation in a mouse model. J. Neuroimaging 32, 617–628. https://doi.org/10.1111/jon.12996.

Pennanen, C., Kivipelto, M., Tuomainen, S., Hartikainen, P., Hänninen, T., Laakso, M.P., Hallikainen, M., Vanhanen, M., Nissinen, A., Helkala, E.L., Vainio, P., Vanninen, R., Partanen, K., Soininen, H., 2004. Hippocampus and entorhinal cortex in mild cognitive impairment and early AD. Neurobiol. Aging 25, 303–310. https://doi.org/10.1016/S0197-4580(03)00084-8.

Petersen, R.C., 2004. Mild cognitive impairment as a diagnostic entity. J. Intern. Med. 256, 183–194. https://doi.org/10.1111/j.1365-2796.2004.01388.x.

Petersen, R.C., Smith, G.E., Waring, S.C., Ivnik, R.J., Tangalos, E.G., Kokmen, E., 1999. Mild cognitive impairment: Clinical characterization and outcome. Arch. Neurol. 56, 303–308. https://doi.org/10.1001/archneur.56.3.303.

Petersen, R.C., Jack, C.R., Xu, Y.-C., Waring, S.C., O'Brien, P.C., Smith, G.E., Ivnik, R.J., Tangalos, E.G., Boeve, B.F., Kokmen, E., 2000. Memory and MRI-based hippocampal volumes in aging and AD. Neurology 54 (3).

Pluta, J.B., Yushkevich, P.A., Das, S.R., Wolk, D.A., 2012. In vivo analysis of hippocampal subfield atrophy in mild cognitive impairment via semi-automatic segmentation of T2- weighted MRI. J. Alzheimer's Dis. 31, 85–99. https://doi.org/10.3233/JAD-2012-111931.In.

Reilly, J.F., Games, D., Rydel, R.E., Freedman, S., Schenk, D., Young, W.G., Morrison, J. H., Bloom, F.E., 2003. Amyloid deposition in the hippocampus and entorhinal cortex: quantitative analysis of a transgenic mouse model. Proc. Natl. Acad. Sci. 100 (8), 4837–4842.

Riek, K., Millward, J.M., Hamann, I., Mueller, S., Pfueller, C.F., Paul, F., Braun, J., Infante-Duarte, C., Sack, I., 2012. Magnetic resonance elastography reveals altered brain viscoelasticity in experimental autoimmune encephalomyelitis. NeuroImage Clin. 1, 81–90. https://doi.org/10.1016/j.nicl.2012.09.003.

Sack, I., Streitberger, K.-J., Krefting, D., Paul, F., Braun, J., Zhan, W., 2011. The influence of physiological aging and atrophy on brain viscoelastic properties in humans. PLoS One 6 (9). https://doi.org/10.1371/journal.pone.0023451.

Sack, I., Jöhrens, K., Wuerfel, J., Braun, J., 2013. Structure-sensitive elastography: on the viscoelastic powerlaw behavior of in vivo human tissue in health and disease. Soft Matter 9, 5672–5680. https://doi.org/10.1039/c3sm50552a.

Scheff, S.W., Price, D.A., Schmitt, F.A., Mufson, E.J., 2006. Hippocampal synaptic loss in early Alzheimer's disease and mild cognitive impairment. Neurobiol. Aging 27, 1372–1384. https://doi.org/10.1016/j.neurobiolaging.2005.09.012.

Scheff, S.W., Price, D.A., Schmitt, F.A., DeKosky, S.T., Mufson, E.J., 2007. Synaptic alterations in CA1 in mild Alzheimer disease and mild cognitive impairment. Neurology 68 (18), 1501–1508.

Schregel, K., Née Tysiak, E.W., Garteiser, P., Gemeinhardt, I., Prozorovski, T., Aktas, O., Merz, H., Petersen, D., Wuerfel, J., Sinkus, R., 2012. Demyelination reduces brain parenchymal stiffness quantified in vivo by magnetic resonance elastography. Proc. Natl. Acad. Sci. U. S. A. 109, 6650–6655. https://doi.org/10.1073/pnas.1200151109.

Schwarb, H., Johnson, C.L., McGarry, M.D.J., Cohen, N.J., 2016. Medial temporal lobe viscoelasticity and relational memory performance. Neuroimage 132, 534–541. https://doi.org/10.1016/j.neuroimage.2016.02.059.

Shahid, S.S., Wen, Q., Risacher, S.L., Farlow, M.R., Unverzagt, F.W., Apostolova, L.G., Foroud, T.M., Zetterberg, H., Blennow, K., Saykin, A.J., Wu, Y.C., 2022. Hippocampal-subfield microstructures and their relation to plasma biomarkers in Alzheimer's disease. Brain 145 (6), 2149–2160.

Sutton, B.P., Noll, D.C., Fessler, J.A., 2003. Fast, iterative image reconstruction for MRI in the presence of field inhomogeneities. IEEE Trans. Med. Imaging 22, 178–188. https://doi.org/10.1109/TMI.2002.808360.

Wisse, L.E.M., Biessels, G.J., Heringa, S.M., Kuijf, H.J., Luijten, P.R., Geerlings, M.I., Group, U.V.C.I.V.C.I.S., 2014. Hippocampal subfield volumes at 7T in early Alzheimer's disease and normal aging. Neurobiol. Aging 35, 2039–2045.

Yassa, M.A., Stark, S.M., Bakker, A., Albert, M.S., Gallagher, M., EL Stark, C., 2010. High-resolution structural and functional MRI of hippocampal CA3 and dentate gyrus in patients with amnestic mild cognitive impairment. Neuroimage 51, 1242–1252. https://doi.org/10.1016/j.neuroimage.2010.03.040.High-resolution.

Ye, B.S., Seo, S.W., Kim, C.H., Jeon, S., Kim, G.H., Noh, Y., Cho, H., Yoon, C.W., Kim, H. J., Jang, E.Y., Lee, J., Kim, J.-H., Chin, J., Lee, J.M., Kim, J.-H., Seong, J.-K., Kim, C.-H., Choe, Y.S., Lee, K.H., Na, D.L., 2014. Hippocampal and cortical atrophy in amyloid-negative mild cognitive impairments: comparison with amyloid-positive mild cognitive impairment. Neurobiol. Aging 35 (2), 291–300.

Yushkevich, P.A., Pluta, J.B., Wang, H., Xie, L., Ding, S.L., Gertje, E.C., Mancuso, L., Kliot, D., Das, S.R., Wolk, D.A., 2015. Automated volumetry and regional thickness analysis of hippocampal subfields and medial temporal cortical structures in mild cognitive impairment. Hum. Brain Mapp. 36, 258–287. https://doi.org/10.1002/hbm.22627.